Astronomy & Astrophysics

The hyperluminous Compton-thick $z \sim 2$ quasar nucleus of the hot DOG W1835+4355 observed by *NuSTAR*

L. Zappacosta[1], E. Piconcelli[1], F. Duras[1,2], C. Vignali[3,4], R. Valiante[1], S. Bianchi[2], A. Bongiorno[1], F. Fiore[1], C. Feruglio[5,6], G. Lanzuisi[3,4], R. Maiolino[7,8], S. Mathur[9,10], G. Miniutti[11], and C. Ricci[12,13,14]

[1] INAF – Osservatorio Astronomico di Roma, via di Frascati 33, 00078 Monte Porzio Catone, Italy
   e-mail: luca.zappacosta@oa-roma.inaf.it
[2] Dipartimento di Matematica e Fisica, Università degli Studi Roma Tre, via della Vasca Navale 84, 00146 Roma, Italy
[3] Dipartimento di Fisica e Astronomia (DIFA), Università di Bologna, via Gobetti 93/2, 40129 Bologna, Italy
[4] INAF – Osservatorio di Astrofisica e Scienza dello Spazio di Bologna, via Gobetti 93/3, 40129 Bologna, Italy
[5] Osservatorio Astronomico di Trieste, Via G.B. Tiepolo 11, 34143 Trieste, Italy
[6] Scuola Normale Superiore, Piazza dei Cavalieri 7, 56126 Pisa, Italy
[7] Cavendish Laboratory, University of Cambridge, 19 J. J. Thomson Ave., Cambridge CB3 0HE, UK
[8] Kavli Institute for Cosmology, University of Cambridge, Madingley Road, Cambridge CB3 0HA, UK
[9] Department of Astronomy, The Ohio State University, 140 West 18th Avenue, Columbus, OH 43210, USA
[10] Center for Cosmology and AstroParticle Physics, The Ohio State University, 191 West Woodruff Avenue, Columbus, OH 43210, USA
[11] Centro de Astrobiología (CSIC-INTA), Depto. de Astrofísica, ESAC Campus, Camino Bajo del Castillo s/n, 28692 Villanueva de la Cañada, Spain
[12] Núcleo de Astronomía de la Facultad de Ingeniería, Universidad Diego Portales, Av. Ejército Libertador 441, Santiago, Chile
[13] Chinese Academy of Sciences South America Center for Astronomy and China-Chile Joint Center for Astronomy, Camino El Observatorio 1515, Las Condes, Santiago, Chile
[14] Kavli Institute for Astronomy and Astrophysics, Peking University, Beijing 100871, PR China

ABSTRACT

We present a 155 ks *NuSTAR* observation of the $z \sim 2$ hot dust-obscured galaxy (hot DOG) W1835+4355. We extracted spectra from the two *NuSTAR* detectors and analyzed them jointly with the archival *XMM-Newton* PN and MOS spectra. We performed a spectroscopic analysis based on both phenomenological and physically motivated models employing toroidal and spherical geometry for the obscurer. In all the modelings, the source exhibits a Compton-thick column density $N_{\rm H} \gtrsim 10^{24}$ cm^{-2}, a 2–10 keV luminosity $L_{2-10} \approx 2 \times 10^{45}$ erg s^{-1}, and a prominent soft excess ($\sim$5–10% of the primary radiative output), which translates into a luminosity $\sim 10^{44}$ erg s^{-1}. We modeled the spectral energy distribution from 1.6 to 850 μm using a clumpy two-phase dusty torus model plus a modified blackbody to account for emission powered by star formation in the far-infrared. We employed several geometrical configurations consistent with those applied in the X-ray analysis. In all cases we obtained a bolometric luminosity $L_{\rm bol} \approx 3-5 \times 10^{47}$ erg s^{-1}, which confirms the hyperluminous nature of this active galactic nucleus. Finally, we estimate a prodigious star formation rate of $\sim$3000 $M_{\odot}$ yr^{-1}, which is consistent with the rates inferred for $z \approx 2-4$ hyperluminous type I quasars. The heavily obscured nature, together with $L_{\rm bol}$, the ratio of X-ray to mid-infrared luminosity, the rest-frame optical morphology, and the host star formation rate are indicative of its evolutionary stage. We can interpret this as a late-stage merger event in the transitional, dust-enshrouded, evolutionary phase eventually leading to an optically bright AGN.

Key words. X-rays: galaxies – galaxies: active – quasars: general – quasars: individual: WISE J1835+4355

1. Introduction

Recent sensitive wide-area mid-infrared ($\sim$3−30 μm; MIR) surveys allowed an almost obscuration-independent selection of rare populations of distant ($z = 2-4$) quasars that are characterized by their huge infrared (IR) output ($L_{\rm IR} \gtrsim 10^{14} L_{\odot}$), which gave them the name hyperluminous infrared galaxies. Using the all-sky survey performed by the Wide-field Infrared Survey Explorer (WISE; Wright et al. 2010), samples of $\sim$100–1000 high-redshift ($z \approx 2-4$) MIR-bright[1] type I and type II hyperluminous sources have been selected according to specific selection criteria (e.g., Weedman et al. 2012; Eisenhardt et al. 2012; Wu et al. 2012). These rare systems are

important as they may provide the clearest view of quasars at the peak epoch of AGN activity ($z \approx 2-3$; Richards et al. 2006; Hopkins et al. 2007; Merloni & Heinz 2008; Delvecchio et al. 2014) and in that they may be a low-redshift analog of the most luminous and massive highest-redshift quasars known (e.g., Fan et al. 2001, 2003; Willott et al. 2010; Bañados et al. 2016). They therefore provide an important testbed to models of supermassive black hole (SMBH) formation and popular AGN/galaxy coevolution scenarios (Silk & Rees 1998; Fabian 1999; King 2003; Volonteri et al. 2006; Hopkins et al. 2008; Kormendy & Ho 2013; Heckman & Best 2014). They may indeed represent different evolutionary phases of popular merger-driven quasar formation scenarios in which the loss of angular momentum of large cold gas reservoirs as a consequence

---

[1] Specifically at observed wavelengths $\gtrsim$10 μm.

of multiple major galaxy encounters causes rapid SMBH growth through infall of chaotic nuclear matter. This triggers powerful AGN activity and generates strong bursts of star formation (Sanders et al. 1988; Di Matteo et al. 2005; Hopkins et al. 2006, 2008; Menci et al. 2008; Narayanan et al. 2010; Treister et al. 2012). A key transitional stage of this process predicts that the dense concentrations of infalling matter will eventually isotropically enshroud the active nucleus, heavily obscuring the sightline to the AGN and causing it to appear red and heavily absorbed at shorter than near-infrared wavelengths (Hopkins et al. 2006; Urrutia et al. 2008; Glikman et al. 2012).

Alternative scenarios involving stochastic short transitional phases of high-matter nuclear accretion flows have also been considered for obscured quasars. They are not connected to major mergers, but are rather linked to minor mergers and episodic cold-gas accretion episodes (flickering AGN scenario; Schawinski et al. 2012, 2015; Farrah et al. 2017).

Observationally obscured AGN are better suited for studying the AGN/galaxy coevolution because they allow the best view of the host galaxy. The most promising $z = 2-4$ AGN candidates for the transitional dust-enshrouded phase are the so-called "hot dust-obscured galaxies" (hot DOGs; Eisenhardt et al. 2012; Wu et al. 2012), that is, sources selected to be bright in the WISE 12 μm (W3) and/or 22 μm (W4) bands and faint or undetected in the 3.4 μm (W1)/4.6 μm (W2) bands (hence called W1W2 drop-out; Eisenhardt et al. 2012). These sources are hyperluminous with $L_{bol} > 10^{47}$ erg s^{-1}, and they are rare (~1000 across the sky; Eisenhardt et al. 2012). They exhibit a peculiar spectral energy distribution (SED) that peaks in the MIR, which suggests that the main source powering these objects is the central AGN and not a powerful starburst. The temperatures derived for their dust reservoir are indeed on the order of $T = 60-100$ K (Wu et al. 2012; Fan et al. 2016b), which is higher than the typical dust temperatures of $T = 30-40$ K in other more common MIR-selected sources such as the normal submillimeter galaxies (e.g., Magnelli et al. 2012) and dust-obscured galaxies (DOGs; Dey et al. 2008). For this reason, they have been dubbed hot DOGs. These sources have been found in regions populated on arcminute scales (~500-700 kpc) by overdense concentrations of submillimeter galaxies, suggesting that they are indeed possible signposts of protocluster regions (Jones et al. 2014). As expected, the few X-ray observations of hot DOGs performed so far showed remarkably clearly that they are luminous and heavily obscured quasars (Stern et al. 2014; Piconcelli et al. 2015; Assef et al. 2016; Ricci et al. 2017a; Vito et al. 2018). In particular, Piconcelli et al. (2015; hereafter P15) found from studying the *XMM-Newton* X-ray spectrum of the hot DOG WISE J183533.71+435549.1 ($z = 2.298$; Wu et al. 2012; hereafter W1835) that the source is reflection dominated and hence obscured by Compton-thick[2] (CT) column densities. This provides further evidence that the source may be in the transitional heavily obscured phase.

We here report on the ~150 ks *NuSTAR* observation of the hot DOG W1835, which provides the first and most obscured *NuSTAR* detection of a $z > 2$ AGN. We perform a broadband ~0.5-20 keV joint *XMM-Newton-NuSTAR* spectral analysis and updated SED modeling.

Throughout the paper we assume a cosmology with $\Omega_\Lambda = 0.73$ and $H_0 = 70$ km s^{-1} Mpc^{-1}. Errors are quoted at 1σ and upper and lower limits at 90% confidence level, unless otherwise stated.

---

[2] The Compton-thick obscuration is formally defined as absorption due to material with a column density of $N_H \geq 1.5 \times 10^{24}$ cm^{-2}.

2. NuSTAR data reduction

The source W1835 was observed with *NuSTAR* (Harrison et al. 2013) for 155 ks (ObsID 60101040002) on 19 November 2015. We removed periods of high 3–20 keV background. The remaining cleaned event files consist of 140 and 143 ks for detectors FPMA and FPMB, respectively. Because the source is expected to be weak and *NuSTAR* has a spatially dependent background (at energies <15–20 keV) given by cosmic unfocused straylight striking the detector through the open design of the telescopes, we chose to completely model the background in the whole detector areas. We employed the *nuskybdg* procedure (Wik et al. 2014). We sampled the background by extracting from each of the four chips in each detector spectra from circular regions of 3–4 arcmin radius. We excluded from these regions the hot DOG position, the chip gaps, and all the point sources detected in the *XMM-Newton*-PN and *XMM-Newton*-MOS images, adopting circular regions with an aperture of radius ~30 arcsec. We then performed a joint modeling of the instrumental FPMA/FPMB and cosmic focused and unfocused (i.e., straylight) backgrounds. From the best fit we reconstructed the background image and checked visually for residual spatial variations in the background-subtracted images. The source is detected in both images at a significance of ~2.5–2.7σ within 20 arcsec radius. The combined significance is 3.3σ. In Fig. 1 we report the combined 3–24 keV FPMA and FPMB images in order to highlight the significance of the hot DOG (blue circle) above the field and compare the *XMM-Newton*-detected point sources in the field (dashed red circles). We then chose the source spectral extraction radius for each detector by simultaneously maximizing the signal-to-noise ratio (S/N) and the net-source counts within increasing apertures (for details, see Zappacosta et al. 2018) centered on the *XMM-Newton*-detected source position (P15). The chosen extraction radii are 30 and 20 arcsec for FPMA and FPMB, respectively. We extracted the spectra from these circular regions using the *nuproduct* task in NuSTARDAS v. 1.4.1 with calibration database (CALDB) v. 20150123. The background spectra within the source spectral extraction regions were simulated from the best-fit model with 100 times the exposure time in order to ensure good statistics for background subtraction.

3. X-ray spectral analysis

The 3–24 keV FPMA and FPMB spectra consist of 40^{+7}_{-6} and 21^{+7}_{-5} background-subtracted counts (which are 24.5% and 24.8% of the total number of counts) whose 1σ uncertainties were estimated assuming Poissonian statistics (Gehrels 1986). The apparent discrepancy between the collected counts in the two detectors is due to the different adopted spectral extraction radii as the *NuSTAR* point spread function encloses in its 30 arcsec aperture (the FPMA extraction region) ~1.5 times more flux than in its 20 arcsec aperture (the FPMB extraction region). We used them jointly with the XMM-PN and the coadded XMM-MOS spectra extracted and produced by P15 from a 42 ks *XMM-Newton* observation (ObsID 0720610101) performed on 18 August 2013. The addition of PN and MOS spectra (106 and 71 net-counts in the 0.5–8 keV band, respectively) allowed us to perform spectral modeling in the broad 0.5–24 keV band. All four spectra were grouped to a minimum of one net-count (i.e., background-subtracted) per bin. We note that *NuSTAR* has 26^{+6}_{-5} (FPMA+FPMB) net-counts compared to 31 ± 0.6 for the XMM-PN and 27^{+6}_{-5} for the XMM-MOS in the common 3–8 keV energy band, and it expands the spectral coverage above the unexplored ~8 keV spectral region (i.e., ~25 keV rest-frame) with another
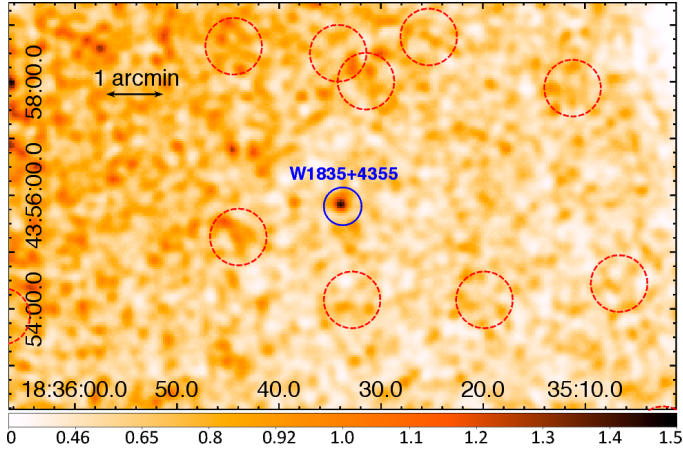
Fig. 1. *NuSTAR* image in equatorial coordinates of the W1835 field in the energy range 3–24 keV (FPMA and FPMB were coadded in order to increase the signal-to-noise ratio). The blue solid 20 arcsec radius circular aperture reports the position of the hot DOG. Red dashed circles report the regions (30 arcsec radius) centered at the position of all the *XMM-Newton*- detected sources in the field (except for W1835) that were removed during the background-modeling procedure. The image was smoothed with a Gaussian kernel of 4 pixels (i.e., 10 arcsec) for better visualization. The color bar reports count/pixel values.

35 source counts up to ~24 keV. We used the Cash statistic (C-stat) as implemented in XSPEC v. 12.8.2 with direct background subtraction (Cash 1979; Wachter et al. 1979).

3.1. Empirical models

In P15 the *XMM-Newton* data alone suggested a best-fit parametrization consisting of a reflection-dominated model. The source was modeled by a cold Compton reflection component model empirically parametrized by a reflector with an infinite plane geometry and infinite optical depth, which also includes the most pronounced fluorescent lines from Fe and Ni K-shell transitions. To this model a soft component consisting of a power law with fixed photon index $\Gamma_{sc} = 2.5$ was added. It accounts for the soft excess over the simple reflection model, which might originate from the primary component that leaked unaltered from the absorber or from photoionized or collisionally ionized or shocked gas (e.g., Guainazzi & Bianchi 2007; Teng & Veilleux 2010; Feruglio et al. 2013). We refer to it as the "scattered component". A further Gaussian component parametrizing the presence of a unresolved ionized Fe transition at 6.7 keV was added in order to account for residuals in the high-energy part of the Fe $K\alpha$ line at 6.4 keV. This may indicate a possible presence of an ionized reflector or a high-temperature collisionally ionized plasma surrounding the active nucleus. The addition of the *NuSTAR* data allows an energy coverage up to observed ~20 keV. This enables us to cover rest-frame energies in the range ~1.6–70 keV and therefore obtain better global constraints on the high-energy part of the spectrum and further shed light on the obscuration state of this quasar. Because of the heavily obscured nature of the source, we properly account for Compton scattering and geometric effects through our modeling. These effects are more pronounced at the highest column densities.

3.1.1. Power-law-based models

We first tried simple models and checked the consistency of the broadband parameterization by comparing it with the parameterization obtained by P15 using *XMM-Newton* data alone.

In our models we always accounted for a multiplicative factor for the possible difference in the calibration between *XMM-Newton* and *NuSTAR* (which has been measured to be no more than 10%; Madsen et al. 2015) and source flux variability that may have occurred between observations. We started with an unabsorbed power-law model. This resulted in a poor fit (C-stat/d.o.f. = 174/157) with a photon index $\Gamma = 0.9 \pm 0.1$ that is consistent with the slope obtained by modeling *XMM-Newton*-only data (P15). The addition of a cold intrinsic absorber (zwabs model in XSPEC) gave $\Gamma \approx 1$ and $N_H \sim 10^{23}$ cm^{-2}, but did not improve the modeling much (C-stat/d.o.f. = 173/156) over the previous parameterization. Strong residuals at the position of the Fe K lines are present. These were interpreted by P15 as due to a prominent neutral Fe Kα line at 6.4 keV with an equivalent width (EW) larger than 1–2 keV, and also due to a ionized Fe line at ~6.67 keV. By fixing $\Gamma = 1.9$, we also obtained high residuals at low energies (1–2 keV). Hence we added a low-energy scattered power-law component whose photon index was tied to that of the primary component. We found a best-fit (C-stat/d.o.f. = 169/156) with $N_H \approx 6 \times 10^{23}$ cm^{-2} and a soft scattered component flux compared to that of the unabsorbed primary (called scattered fraction[3], hereafter f_{sc}), which is in the 1σ range $f_{sc} \approx 10-20\%$. This is significantly higher than normally found for heavily absorbed AGN (e.g., Brightman et al. 2014; Lanzuisi et al. 2015). Leaving Γ free to vary did not improve our modeling signficantly. The addition of two unresolved Gaussian lines to account for the neutral and ionized Fe lines further improved our fit (C-stat/d.o.f. = 147/154), giving a column density $N_H = 1.4^{+0.7}_{-0.5} \times 10^{24}$ cm^{-2} that is compatible with CT absorption. We further modified the absorber by accounting for Compton scattering of X-ray photons using the multiplicative cabs model. This model accounts for scattering of photons outside of the line of sight (therefore neglecting photons that scatter into the line of sight). Compton scattering at the highest column densities is a non-negligible effect and further suppresses the level of the primary continuum at a fixed column density. This leads to an almost unaltered best-fit parameterization that we refer to as model CAbsPow with the exception of the scattered fraction, which resulted in a more reasonable $f_{sc} = 5^{+4}_{-3}\%$. The 2–10 keV and 10–40 keV unabsorbed luminosities are $L_{2-10} = 2.9 \times 10^{45}$ erg s^{-1} and $L_{10-40} = 1.9 \times 10^{45}$ erg s^{-1}. A summary of the parameters derived by our spectral analysis is given in Table 1.

3.1.2. Modeling scattering and reflection from dense medium

The presence of the neutral Fe line suggests the existence of an additional reflection component that still must be accounted for. In addition to a primary power-law component modified by photoelectric absorption and Compton scattering, we therefore modeled the spectrum by employing a reflection component including spectral features from neutral Fe and Ni at 6–7 keV parameterized by the pexmon model (Nandra et al. 2007) and a 6.65 keV (best fit from *XMM-Newton* spectra alone, see P15) line for the ionized Fe line at ~6.67 keV. The reflection model assumes an infinite planar geometry with infinite optical depth illuminated by the primary continuum and subtending for an isotropic source an angle of $\Omega = 2\pi \times R$, where R is the reflection parameter. In the model we assumed solar abundance, an exponential energy cutoff for the incident primary power-law $E_c = 200$ keV (Fabian et al. 2015), and a reflector inclination

---

[3] Given the Γ tied between the scattered and primary power-law components, we calculated it as the ratio between the model normalizations.

Table 1. X-ray spectral fitting: derived parameters.

Model[a]	C-stat/d.o.f.	Γ	$N_{\rm H}$ $(10^{24}\,{\rm cm}^{-2})$	$\Gamma_{\rm sc}$	$f_{\rm sc}$ (%)	L_{2-10} $(10^{45}\,{\rm erg\,s}^{-1})$	L_{10-40} $(10^{45}\,{\rm erg\,s}^{-1})$
CAbsPow[b]	147/154	(1.9)	$1.4^{+0.7}_{-0.5}$	$(=\Gamma)$	5^{+4}_{-3}	$2.9^{+3.6}_{-1.3}$	$1.9^{+2.4}_{-0.9}$
ReflDom[c]	149/156	(1.9)	–	$(=\Gamma_{\rm pexmon})$	(2)	0.2^{f}	0.6^{f}
MYTor[d]	149/155	(1.9)	$1.1^{+0.5}_{-0.3}$	$(=\Gamma)$	9^{+5}_{-3}	$1.6^{+0.9}_{-0.5}$	$1.0^{+0.6}_{-0.6}$
BNSphere[e]	149/155	(1.9)	$0.9^{+0.3}_{-0.2}$	$(=\Gamma)$	15^{+6}_{-4}	$0.9^{+0.3}_{-0.2}$	$0.6^{+0.2}_{-0.2}$

Notes. [a] See Sects. 3.1, 3.1.1 and 3.2. [b] WABS(ZPOWERLW$_{\rm sc}$+ZWABS*CABS*ZPOWERLW+ZGAUSS$^{\rm neut}_{FeK\alpha}$+ZGAUSS$^{\rm ion}_{FeK\alpha}$), where ZGAUSS$^{\rm neut}_{FeK\alpha}$, ZGAUSS$^{\rm ion}_{FeK\alpha}$ are Gaussian lines to parametrize the neutral and ionized Fe Kα line; [c] WABS(ZPOWERLW$_{\rm sc}$+ZGAUSS$^{\rm ion}_{FeK\alpha}$+PEXMON); [d] WABS(ZPOWERLW$_{\rm sc}$+ ZPOWERLW*MYTZ+MYTS+MYTL); [e] WABS(ZPOWERLW$_{\rm sc}$+BNTORUS); [f] observed luminosity not corrected for absorption.

angle of 60 deg (default in XSPEC). We further added a soft-excess component parameterized as a power law with photon index tied to that of the primary component. In order to decrease the number of free parameters, we set its flux to be 2% of the primary flux, as is commonly found in heavily obscured ($N_{\rm H} \gtrsim 10^{23}\,{\rm cm}^{-2}$) AGN (e.g., Lanzuisi et al. 2015). We obtain a best fit with a primary component completely suppressed by $N_{\rm H} \gg 10^{25}\,{\rm cm}^{-2}$ and in which only the scattered and reflection components effectively contribute to the modeling[4]. A more accurate treatment of scattering and reflection in high dense medium is performed by exploiting physically motivated toroidal models in Sect. 3.2.

The primary component is heavily obscured, therefore we tried to model the spectrum assuming a reflection-dominated scenario in which the coronal component is completely absorbed. Hence we removed the absorbed power-law component from our model. In our parameterization we linked the power-law slope and normalization of the PEXMON and scattered power-law. We therefore assumed that the scattered component is composed of coronal flux leaking through the obscurer unabsorbed (i.e., assuming a patchy obscurer distribution). We furthermore assumed that the scattered flux is 2% of the primary, giving rise to the reflected component. The resulting best-fit parameterization (model ReflDom) constitutes an equally good yet simpler parametrization to the data with C-stat/d.o.f. = 149/156. This confirms that the primary absorbed component is not required to parameterize our data. Leaving Γ free to vary does not significantly improve the parameterization (C-stat/d.o.f. = 148/155). The observed 2–10 keV and 10–40 keV luminosities from the reflected component are $L_{2-10} = 2.4 \times 10^{44}\,{\rm erg\,s}^{-1}$ and $L_{10-40} = 5.7 \times 10^{44}\,{\rm erg\,s}^{-1}$, respectively. When we assume a column density $N_{\rm H} \approx 10^{25}\,{\rm cm}^{-2}$ of the obscuring material, the unobscured X-ray luminosity is a factor of ~100 and ~10 higher, respectively.

3.2. Geometry-dependent models

In order to obtain more accurate and physically motivated constraints, we used MYTorus (Murphy & Yaqoob 2009; Yaqoob 2012), which is a Monte Carlo model based on a toroidal circumnuclear structure that absorbs and reprocesses the primary radiation self-consistently and accounts for geometric effects, Compton scattering for radiation propagating toward high column density medium, and reflection and fluorescent line emission in the reprocessed radiation. The torus has a half-opening angle of 60 deg and is composed of uniform and neutral material.

An input power-law incident primary radiation is assumed. Its implementation in XSPEC consists of three different table model components: (1) one for the attenuation of the line-of-sight radiation due to photoelectric and Compton-scattering effects (MYTZ); (2) one to reprocess the radiation due to reflected radiation into the line of sight (MYTS); (3) and one that calculates the contribution from scattered line emission (MYTL). We combined all the three components by linking the column density and setting the relative normalization constants of each component to unity. We furthermore added a power law to account for the scattered flux at soft energies and for the ionized Fe line.

Because of the high column density and in order to comply with the geometrical requirements invoked by the standard unification schemes in which type II sources are seen at high inclinations, an almost edge-on view of the torus of 85 deg was assumed (Brightman et al. 2014; Lanzuisi et al. 2015; Zappacosta et al. 2018). We also fixed $\Gamma = 1.9$ and tied to it the photon index for the scattered component. We fixed the normalizations of MYTS ($A_{\rm S}$) and MYTL ($A_{\rm L}$) relative to (MYTZ) to unity and linked all the components to the same equatorial column density $N^{\rm eq}_{\rm H}$. The latter is related to the line-of-sight column density $N_{\rm H}$ according to the inclination angle assumed and in this almost edge-on case follows the relation: $N_{\rm H} \simeq 0.98\,N^{\rm eq}_{\rm H}$.

The best fit (C-stat/d.o.f. = 149/155) with this model (model MYTor) is reported in Fig. 2. In the left panel we report XMM-Newton and NuSTAR unfolded spectra along with the best-fit model. The right panel shows the different subcomponents contributing to the incident model. The column density estimated with this model is $N_{\rm H} = 1.1^{+0.5}_{-0.3} \times 10^{24}\,{\rm cm}^{-2}$. The scattered fraction is measured to be $f_{\rm sc} = 9^{+5}_{-3}\%$, which, although slightly on the high side, is consistent within the errors with the typical fractions for highly absorbed ($N_{\rm H} > 10^{23}\,{\rm cm}^{-2}$) AGN. This fraction in our parameterization is highly degenerate with the column density. This is shown by the confidence contours reported in Fig. 3 for the two interesting parameters[5]. Given this parameterization, the 2–10 keV and 10–40 keV unabsorbed luminosities are $L_{2-10} = 1.6 \times 10^{45}\,{\rm erg\,s}^{-1}$ and $L_{10-40} = 1.0 \times 10^{45}\,{\rm erg\,s}^{-1}$, respectively.

---

[4] We verified that the derived column density is insensitive to the particular choice of inclination angle.

[5] We note that the assumed high-inclination angle is conservative in terms of $N_{\rm H}$ as it gives lower values than lower inclination angles. Furthermore, it does not affect the maximum allowed value of the scattered fractions, but it affects its constraints at the lower-end values. For instance, assuming an inclination angle of 70 deg, we obtain a 90% lower limit of $N_{\rm H} \sim 7 \times 10^{23}\,{\rm cm}^{-2}$ and $f_{\rm s} = 0.7–22\%$ (1σ range). However, as for all inclinations angles $\lesssim 70–80$ deg, the derived uncertainties are affected by the maximum tabulated $N_{\rm H} = 10^{25}\,{\rm cm}^{-2}$ in the MYTorus model, which prevents an accurate and correct sampling of the entire parameter space of interest.
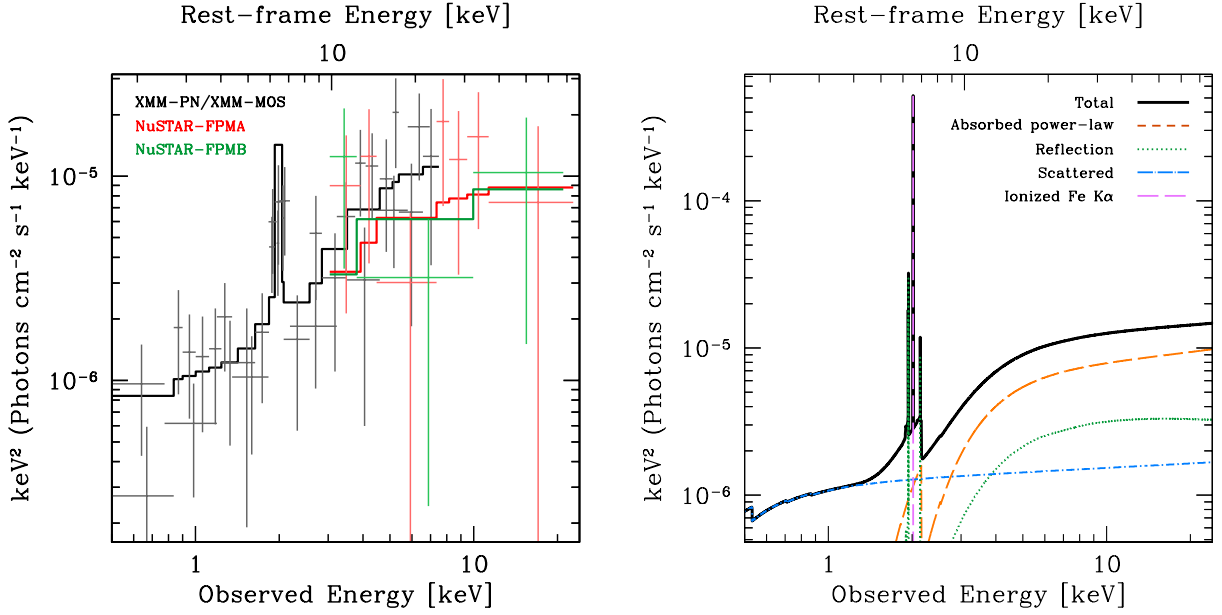
Fig. 2. *Left panel*: *XMM-Newton* and *NuSTAR* broadband 0.5–24 keV unfolded spectrum of W1835 grouped at a minimum of five net-counts per bin for better visual representation. The black, red, and green thick solid lines are the best-fit MYTor unfolded model (as reported in Table 1 and discussed in Sect. 3.2) for *XMM-Newton*-PN, *NuSTAR*-FPMA, and *NuSTAR*-FPMB, respectively. Data are reported in lighter colors. At low energy we omit the *XMM-Newton*-MOS best-fit model for clarity and report MOS and PN spectra with the same color. *Right panel*: corresponding best-fit theoretical model (thick solid black line) and subcomponents (discontinuous lines). The absorbed primary power-law, the reflection, and the scattered components are reported with dashed orange, dotted green, and dash-dotted blue lines. The magenta dashed line indicates the ionized Fe line.

This model was not previously evaluated in P15 for the *XMM-Newton* data alone. The inclusion of the *NuSTAR* data allows us to confirm the *XMM-Newton* estimated values (which crucially depend on the level of the *XMM-Newton* higher energy bins, which, being in a regime of low S/N, may suffer from systematics) and to better define the upper-end value on N_H as reported in Fig. 3.

Hot DOGs are usually considered a transitional dust-enshrouded/highly star-forming phase in the merger-driven quasar formation scenario (Sanders et al. 1988; Hopkins et al. 2008; Wu et al. 2012). In this scenario, the accretion of matter proceeds through intense and chaotic accretion phases caused by the loss of angular momentum resulting from major mergers as opposed to more moderate accretion states typical of the secularly evolving planar geometries (disk-torus structure) invoked in unified models (e.g., Urry & Padovani 1995). In this case, we expect that in the former the obscuring material is distributed more isotropically than in the toroidal structures that are typically invoked for more standard, Seyfert-like sources. If this is the true scenario for W1835, it is reasonable to evaluate a model in which the obscurer covers the entire sphere, regardless of its distance from the nucleus. We employed a specific table model derived from Monte Carlo based calculations for a homogeneous toroidal obscurer modeled as a sphere in which there is a biconical cavity with variable opening angle (hereafter BNTorus; Brightman & Nandra 2011). We used the case with an opening angle of 0 deg (i.e., no biconical openings) and hence with a spherical obscurer distribution (i.e., isotropic obscuration; model BNSphere). This model, as well as MYTorus, assumes a homogeneous matter distribution, but this is a probably good approximation of the spherical high covering factor obscuration scenario, even if there may likely be inhomogeneities in the gas/dust distribution (possibly with some sight-lines exhibiting Compton-thin column densities). This model is simpler than MYTor as it involves the same number of free parameters and does not need any inclination angle assumption. We obtain a best-fit (C-stat/d.o.f. = 149/155) column density of $N_H = 0.9^{+0.3}_{-0.2} \times 10^{24}$ cm^{-2} with a slightly higher scattered fraction $f_{sc} = 15^{+6}_{-4}\%$ (assuming $\Gamma = 1.9$ and $Z = 1 Z_\odot$). Confidence contours for this case are reported in red in Fig. 3. The degeneracy of the two parameters is less pronounced than for the MYTor case, but the scattered fraction is rather high, as shown by the comparison with highly obscured/CT AGN candidates reported from the COSMOS survey in Lanzuisi et al. (2015). However, the increase in f_{sc} is expected because in BNSphere the low-energy nuclear radiation can not escape or scatter outside of the nuclear region without being obscured. Therefore, if the source truly is dust enshrouded, the soft-excess emission must come from elsewhere. The derived parameters for both MYTor and BNSphere modelings are reported in Table 1.

We expect that most of the CT absorption occurs in the innermost galactic regions around the AGN, as argued by Buchner & Bauer (2017). However, as stressed by these authors, their study is valid for the AGN population at large, and peculiar/rare sources such as hot DOGs are therefore not sampled. This means that we cannot make any strong conclusion on the location of the CT absorber in W1835.

4. Modeling the optical-to-infrared SED

In order to have the most complete view of W1835, P15 performed SED fitting based on ten photometric points covering the MIR to far-infrared (FIR) wavelength range collected from the literature. Their SED modeling included both a galactic starburst and nuclear emission components. In particular for the latter, they used a grid of smooth torus models with a flared-disk geometry (Fritz et al. 2006; Feltre et al. 2012). The galactic component at longer wavelengths was well parameterized with
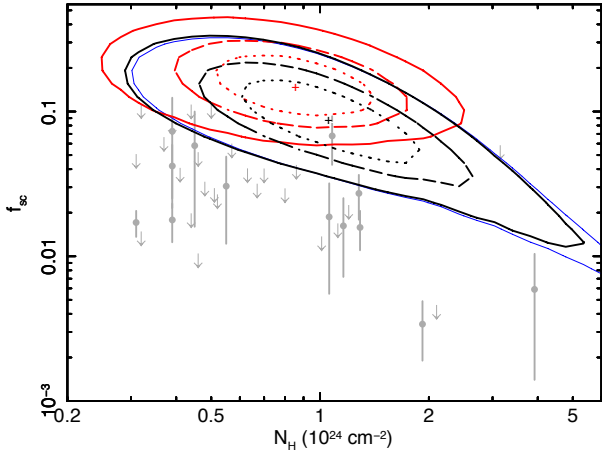
Fig. 3. Confidence contours for $f_{\rm sc}$ and $N_{\rm H}$ in MYTor modeling (black) and the BNSphere model (red). Dotted, dashed, and solid lines represent contours for 68%, 90%, and 99% confidence levels. Thick contours represent constraints from the joint *XMM-Newton-NuSTAR* modeling. The thin solid blue contour reports 99% constraints from *XMM-Newton*-only spectral analysis. Gray data indicate the scattered fractions for the heavily absorbed and CT AGN selected in the XMM-COSMOS field (Lanzuisi et al. 2015, errors and upper limits are 90% c.l.).

Table 2. Photometric points of W1835.

Instrument	Band	Flux density
HST/WFC3 F160W	1.6 μm	12.8 $\pm$ 0.9 μJy
Spitzer IRAC1	3.6 μm	51.5 $\pm$ 2.2 μJy
Spitzer IRAC2	4.5 μm	142.8 $\pm$ 3.0 μJy
WISE W3	12 μm	6790 $\pm$ 190 μJy
WISE W4	22 μm	24.6 $\pm$ 1.0 mJy
Herschel PACS	70 μm	53.6 $\pm$ 4.2 mJy
Herschel PACS	160 μm	92.8 $\pm$ 17.1 mJy
Herschel SPIRE	250 μm	81.0 $\pm$ 8.1 mJy
Herschel SPIRE	350 μm	72.0 $\pm$ 7.2 mJy
Herschel SPIRE	500 μm	33.0 $\pm$ 3.3 mJy
SCUBA-2	850 μm	8.0 $\pm$ 1.5 mJy

Notes. All photometric points are from P15, except for the HST/WFC3 point (Farrah et al. 2017) and the *Herschel* PACS points (IRSA).

either the Arp 220 template or with a optically thin approximation of a modified blackbody with fixed emissivity index $\beta = 2$. From the latter, the authors obtained a temperature $T_{\rm dust} \approx 40$ K for the dust component. This temperature is lower than those estimated by Fan et al. (2016b) and Wu et al. (2012), that is, $T_{\rm dust} \approx 70$ K and $T_{\rm dust} \approx 90$ K, respectively. Furthermore, it is lower than the typical hot DOG temperatures and compatible with the highest temperature for normal DOGs and with the maximum temperatures derived by dust heated by stellar processes (e.g., Magnelli et al. 2012; Wu et al. 2012). Here we perform an improved SED fitting using updated photometric points from the *Herschel* catalog in the NASA/IPAC Infrared Science Archive (IRSA) and adding HST/WFC3 F160W band photometry at 1.6 μm with refined modeling that accounts for the clumpy circum-nuclear torus. Table 2 reports the photometric points considered for the SED modeling.

The approach we followed is based on a two-component fitting procedure recently developed and employed in type I hyper-

luminous sources by Duras et al. (2017). In this procedure the SED is fit with a combination of quasar and host galaxy templates. The AGN component is described as the superposition of the accretion disk emission and of the radiation coming from the dusty torus. We built a library of templates for the quasar emission using the broken power-law description by Feltre et al. (2012) for the accretion disk and the model by Stalevski et al. (2016) for a clumpy two-phase dusty torus characterized by high-density clumps embedded in a low-density and smooth medium. The two were appropriately normalized to preserve the energy balance between the ultraviolet and the IR bands. The library is composed of about 7200 templates with different values of the optical depth at 9.7 μm, the inclination along the line of sight (from 50 to 90 deg, in order to force a type II configuration in which the direct view of the SMBH is blocked by the torus) and the dust geometry and distribution. The second component of the model is a modified blackbody that accounts for the emission powered by star formation that is absorbed and then re-emitted by the surrounding dust in the MIR and FIR bands. We parameterized it as

$$S_\lambda \propto (1 - {\rm e}^{-\tau_\lambda}) B_\lambda(T_{\rm dust}),$$

where $B_\lambda(T_{\rm dust})$ is the blackbody model and $\tau_\lambda = (\lambda_0/\lambda)^\beta$, is the optical depth, which is assumed to have a power-law dependence, with λ_0 being the wavelength at which the optical depth reaches unity and β being the dust emissivity index. Because we only have a small number of photometric points, we fixed $\beta = 1.6$, which seems to be the most reliable value for both local and high-z quasars (Beelen et al. 2006; Bianchi et al. 2017) and $\lambda_0 = 125$ Å (Huang et al. 2014; Fan et al. 2016b). The cold-dust library consists of 70 templates with a range of temperatures from 30 to 100 K.

In Fig. 4 we show the rest-frame optical-to-FIR SED with the best-fit model (solid line). The accretion disk plus torus emission is shown in blue and the cold-dust emission in red. The black line is the total best-fit model emission. From this best fit we were able to derive some physical quantities of both the host galaxy and the nuclear source. They are reported in Table 3. The intrinsic quasar bolometric luminosity was computed by integrating the emission coming from the AGN component from 1 up to 1000 μm and rescaling it by a factor ~1.7 to account for geometry and anisotropy of the radiation field caused by the obscurer geometry and its orientation (Pozzi et al. 2007). This correction is an average value computed for a sample of quasars characterized by a toroidal obscurer and moderate degree of obscuration (log[$N_{\rm H}/{\rm cm}^{-2}$] $\approx 10^{22}$–$10^{23.4}$ cm^{-2}). If the emitting dust is also responsible for the CT obscuration and if a spherical geometry is in place, we should expect larger corrections and therefore possibly higher bolometric luminosities. The IR luminosity ($L_{\rm IR}$) of the host, a tracer of the reprocessed UV stellar light, is obtained by integrating the dust emission component in the range 8–1000 μm and is $L_{\rm IR} = 7.3 \times 10^{46}$ erg s^{-1}. From this we computed the star formation rate (SFR) using the relation by Kennicutt (1998) scaled to a Salpeter initial mass function, gaining an extremely high value of SFR of about $SFR = 3300 \pm 100 \, M_\odot$ yr^{-1}. The best-fit dust emission shows a temperature of about $T_{\rm dust} = 69$ K, in good agreement with the estimates by Fan et al. (2016b). Our estimates differ substantially from the $SFR \approx 2100 \, M_\odot$ yr^{-1} and $T_{\rm dust} \approx 40$ K reported by P15. We verified that this difference is mainly driven by the adoption of the modified blackbody model that in P15 was approximated assuming the optically thin regime and adopting $\beta = 2$. The inferred dust mass of $(3-4) \times 10^8 \, M_\odot$ (estimated as in Beelen et al. 2006, see Table 3) is consistent with
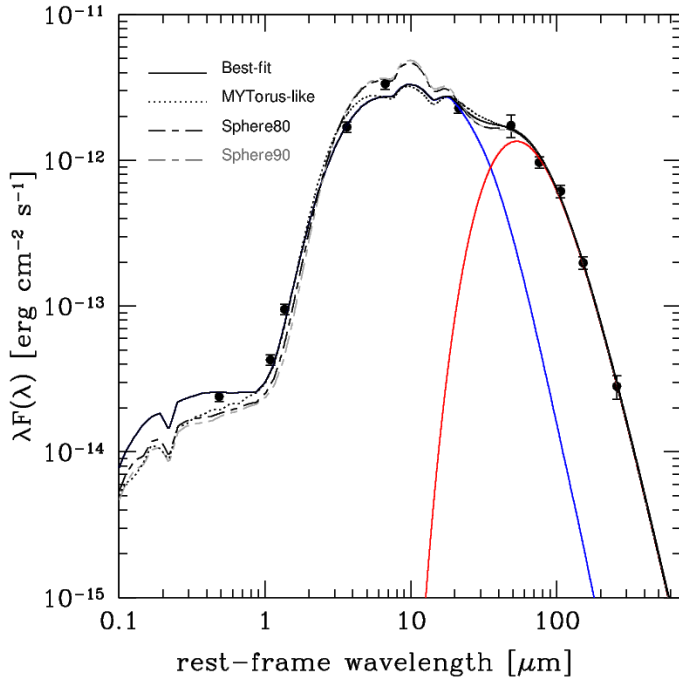
Fig. 4. SED modeling for W1835. The solid line reports the best-fit model (black, red, and blue represent the total, AGN-only, and modified blackbody components). Dotted and dashed lines represent best-fit models assuming a toroidal geometry similar to the MYTor and BNSphere (black and gray show 80 deg and 90 deg inclination angles) models used for the X-ray analysis (Sect. 3.2). See Sect. 4 and Table 3 for further details.

typical abundances in other hot DOGs (Fan et al. 2016b) and in coeval and higher redshift type I analogs (e.g., Beelen et al. 2006; Valiante et al. 2014; Duras et al. 2017).

In order to be consistent with the toroidal models used in our X-ray analysis, we tried to model the SED by forcing similar torus parameters. To approximate the MYTorus geometry (i.e., MYTorus-*like*), we fixed the same torus opening angle and allowed inclinations in the range 70–90 deg. We also tried an almost fully covered obscurer (i.e., *Sphere80*) by adopting the templates with only a polar cap of 10 degrees left open and a 80-degree inclination (almost edge-on)[6]. We obtained reasonable parameterizations although with a slightly worse χ^2. The very high obscuration of the quasar and the HST/WFC3 F160W image (Fan et al. 2016a; Farrah et al. 2017), which shows a somewhat extended and irregular host emission, means that the emission shortward of ∼1 μm is very likely partially contributed by the host. In our models we tried to account for a maximum contribution from the AGN that does not include the host. Temperatures and derived SFR are in the range $T_{dust} \approx 60$–70 K and around $SFR \approx 3000\,M_\odot\,\text{yr}^{-1}$, respectively, hence not very dissimilar from the estimate from the best-fit parameterization (see Table 3 for detailed estimates). In Fig. 4 we report the best-fit parameterizations for the MYTorus-like (dotted) and *Sphere80* (dashed) cases. We tried a fully covered (4π) obscurer (i.e., *Sphere90*) and report it as the gray dashed line in Fig. 4. The spherical parameterizations slightly underestimate the photometric points around of 1 μm rest-frame. This is expected, and

---

[6] Compared to the smooth toroidal models used in our X-ray analysis, those used in the SED fitting are clumpy. Furthermore, the disk geometry for the latter is a conical torus (flared disk), while in MYTorus, a donut-shaped torus is assumed.

because of the extremely obscured nature of this source, these points can therefore be interpreted to be contributed by the stellar emission from the host, which is not accounted for in our modeling.

In the HST/WFC3 F160W image a low surface brightness contribution from the stellar host is visible (Fan et al. 2016a; Farrah et al. 2017). To infer its level, we included an additional component using ∼900 galaxy templates from Bruzual & Charlot (2003), with different levels of extinction spanning the range $\Delta E(B-V) = 0$–0.5 and assuming a Chabrier (2003) initial mass function. We find a fractional contribution of $f_{host} \approx 58$–75% (90% confidence level interval) in the optical rest-frame band (i.e., in the Johnson B band). Despite this, the global AGN and dust properties remain remarkably consistent with the values reported in Table 3. However, the HST/WFC3 F160W photometric point is the only optical constraint to the host template in the SED modeling. At shorter wavelengths, the uncertainties at 90% level in f_{host} become much larger. In addition, systematics may likely be affecting the derived value. More data at bluer rest-frame wavelengths are required to remove possible systematics and reduce the uncertainty on the host contribution.

5. Discussion

5.1. Confirming high obscuration and high luminosity

Our analysis confirms that W1835 hosts a luminous and heavily obscured quasar. An empirical parameterization accounting separately for different primary and reflection components suggests mild to heavy CT obscuration. A model with a reflection-only component can already provide an excellent description of the data. Physically motivated models implementing a toroidal or spherical geometry for the obscurer and accounting for Compton-scattering effects give column densities at around $\sim 10^{24}\,\text{cm}^{-2}$, that is, somewhat lower than the formal threshold defining a source CT (i.e., $N_H = 1.5 \times 10^{24}\,\text{cm}^{-2}$). However, (i) they require scattered fractions of $f_{sc} \gtrsim 5$–9%, which is slightly on the high side but still consistent within the errors, except for BNSphere ($f_{sc} \approx 15\%$), with the canonical observed few-percent values (see Sect. 5.2 for further details) and (ii) the scattered fractions and column density are anticorrelated. A CT obscuration with more moderate fractions is therefore very likely (i.e., at 1σ level, see Fig. 3). To our knowledge, W1835 is the most obscured, most luminous high-redshift AGN detected by *NuSTAR*. Other known hot DOGs whose low-energy X-ray spectra were analyzed exhibit values of $N_H \approx 6$–$7 \times 10^{23}\,\text{cm}^{-2}$, although with large uncertainties (Assef et al. 2016; Ricci et al. 2017a). An exception is W0116 − 0505 (hereafter W0116), one of the X-ray brightest hot DOGs that has a column density similar to that of W1835 (Vito et al. 2018). Recently, Goulding et al. (2018) analyzed the X-ray emission of a sample of extremely red hyperluminous quasars (ERQ) at $z = 1.5$–3.2, finding indication of heavy absorption ($N_H \gtrsim 10^{23}\,\text{cm}^{-2}$). Through spectral analysis of the stacked spectrum of the most weakly detected *Chandra* sources, they estimated column densities on the order of $N_H \sim 10^{24}\,\text{cm}^{-2}$.

The derived unabsorbed luminosities for W1835 are on the order of $L_X \approx 10^{45}\,\text{erg s}^{-1}$ (see Table 1). Based on this and on the estimated bolometric luminosities (Table 3), we can derive the bolometric corrections $k_{bol,X} = L_X/L_{bol}$ in the 2–10 keV and 10–40 keV bands. By assuming as fiducial models the MYTor X-ray parameterization and the best-fit SED modeling, we obtain $k_{bol,2-10} \approx 270$ and $k_{bol,10-40} \approx 440$. If we consistently (to the X-ray model) assume a MYTorus-like toroidal structure for the

Table 3. SED modelings: derived quantities.

Model	χ_r^2	θ_{oa} (deg)	i (deg)	$T_{dust}{}^a$ (K)	$L_{IR}{}^b$ (erg s^{-1})	L_{bol} (erg s^{-1})	$L_{6\,\mu m}$ (erg s^{-1})	SFR ($M_\odot$ yr^{-1})	Dust mass^c ($10^8\,M_\odot$)
Best fit	1.44	30	70	69	7.3×10^{46}	4.39×10^{47}	1.13×10^{47}	3300^{+100}_{-100}	3.9
MYTorus-like	2.06	(60)	70	63	6.0×10^{46}	4.71×10^{47}	1.07×10^{47}	2700^{+200}_{-150}	3.2
Sphere80	4.51	(10)	(80)	69	7.3×10^{46}	5.32×10^{47}	1.42×10^{47}	3300^{+200}_{-200}	3.9
Sphere90 (edge-on)	6.56	(10)	(90)	67	6.9×10^{46}	5.13×10^{47}	1.38×10^{47}	3100^{+100}_{-100}	3.7

Notes. Quantities reported in parentheses have been assumed fixed during the modeling. $^{(a)}$ The typical uncertainty on the temperature is ± 5 K. $^{(b)}$ Relative to the dust emission component. $^{(c)}$ Calculated as in Beelen et al. (2006).

SED modeling, we obtain similar values, that is, a factor ~1.1 larger. These values are all in agreement with bolometric corrections found for X-WISSH sample of $z = 2$–4 type I hyperluminous MIR/optically selected quasars (e.g., Martocchia et al. 2017) and with the extrapolated trend from less luminous type II AGN (e.g. Lusso et al. 2012).

Luminous optically bright quasars have been found to exhibit X-ray luminosities weaker than those inferred by a linear extrapolation from X-ray selected lower-luminosity AGN (Gandhi et al. 2009; Mateos et al. 2015) and are more in line, but still weaker, than extrapolations from dust-obscured galaxies at lower luminosities (Fiore et al. 2009; Lanzuisi et al. 2009). The X-WISSH quasars, which are the most luminous type I AGN in the universe, clearly show this X-ray weakness compared to their MIR radiative output (Martocchia et al. 2017). Recently revised nonlinear relations between X-ray and MIR intrinsic luminosities have been derived by Stern (2015) and Chen et al. (2017) in order to account for the observed X-ray weakness exhibited at the highest luminosities. Ricci et al. (2017a), considering a sample of X-ray detected hot DOGs for which spectroscopic analysis is possible (including W1835), reported L_{2-10} significantly lower than those reported by the X-WISSH sources that exhibit comparable $L_{6\,\mu m}$. This has been considered as evidence of further intrinsic X-ray weakness or significant underestimation of the column density. A somewhat opposite behavior has been reported by Vito et al. (2018) for the hot DOG W0116, for which L_{2-10} appears to be comparatively higher than the extrapolated trends from hyperluminous quasars (i.e., somewhat X-ray louder). As reported by Vito et al. (2018), $L_{6\,\mu m}$ for this source might be underestimated given that it has been computed under the assumption of isotropic emission (Tsai et al. 2015; Vito et al. 2018). In order to understand the level of underestimation and to consistently compare W0116 to our results for W1835, we performed SED fitting for W0116 using the photometric points provided by Tsai et al. 2015, see their Table 2). From our best-fit model we obtain $L_{6\,\mu m} = 1.5 \times 10^{47}$ erg s^{-1}, that is, a factor >4 higher than the values used by Vito et al. (2018). With this new estimate we find W0116 in line with the X-ray-to-MIR luminosity values reported for type I quasars. Similarly, the spectral analysis on the X-ray stacked spectrum of weak ERQs performed by Goulding et al. (2018) gives a value of the intrinsic X-ray luminosity that agrees with the expected $L_{6\,\mu m}$ for hyperluminous type I AGN. Even in this case, anysotropic MIR emission could cause an underestimation of the true MIR luminosity. In this case, we would expect these sources to exhibit slightly lower X-ray radiative outputs (by a factor of a few) than the higher MIR luminosities, as suggested by Goulding et al. (2018) themselves.

In Fig. 5 we report the X-ray-to-MIR luminosity for the W1835 (red circle), the Ricci et al. hot DOGs sample (blue filled triangles), W0116 (magenta squares empty and filled, the latter being plotted with our SED-derived $L_{6\,\mu m}$), the X-WISSH sources (stars), two reddened quasars (green empty triangles; Feruglio et al. 2014; Banerji et al. 2015; Martocchia et al. 2017), and the measure from the stacked ERQ spectrum by Goulding et al. (2018; orange diamond). We also report X-ray-to-MIR relations obtained from MIR-selected AGN (Lanzuisi et al. 2009; Fiore et al. 2009), X-ray selected AGN (Mateos et al. 2015; Chen et al. 2017), and specifically tuned for the hyperluminous regime (Stern 2015). We note that W1835 lies higher than the average hot DOGs locus found by Ricci et al. (2017a) and close to W0116 and the heavily absorbed ERQs and is consistent with the lower portion of the type I quasars and the red quasars. Hence it exhibits a lower degree of X-ray weakness, at least similar to that inferred for type I luminous AGN.

5.2. Origin of the soft excess

In low-count spectra, the soft-excess component is usually reproduced by a single power-law component. If forced to have the same photon index as the primary intrinsic continuum, this component parameterizes an absorber in which the primary flux leaks (or Thomson scatters) unaltered through it. This parameterization is a convenient way to include a soft component by adding only one free parameter to the model and have a reference measure of f_{sc}. Given the highly obscured nature of W1835, the relatively high soft-excess emission may include additional components that are not directly linked to the quasar emission itself.

From our SED fitting we find that the host of this AGN harbors powerful stellar nurseries capable of producing stars at a rate of ~3000 $M_\odot$ yr^{-1}. These levels of star formation are typical of other hyperluminous high-redshift quasars (e.g., Fan et al. 2016b; Duras et al. 2017). The scattered flux may therefore be contributed by X-rays from powerful star-forming regions such as are found in local galaxies (Ranalli et al. 2003). If we assume $SFR = 2000$–$3000\,M_\odot$ yr^{-1}, we can estimate the expected 2–10 keV luminosity using the Ranalli et al. (2003) relation (updated by Kennicutt & Evans 2012) and obtain $L_{2-10}^{SF} \approx 1.2 \times 10^{43}$ erg s^{-1}, which is ~10% of the estimated scattered flux (Table 1). This does not significantly account for the soft excess, especially for the BNSphere model, whose estimated column density depends very little on f_{sc} (see Fig. 3). Therefore the BNSphere model is not an adequate parameterization for the obscurer. This would imply either a patchy 4π obscurer with different properties from the more local sources (in terms of geometry, covering factor, and line-of-sight N_H) or a more standard torus-like geometry. Alternatively, it would require a different soft X-ray contributor than is normally invoked for a more local source.

Other possible contributors to this emission are photoionized gas, which is typically observed in local AGN (Bianchi et al. 2006; Guainazzi & Bianchi 2007), or galaxy-scale collisionally
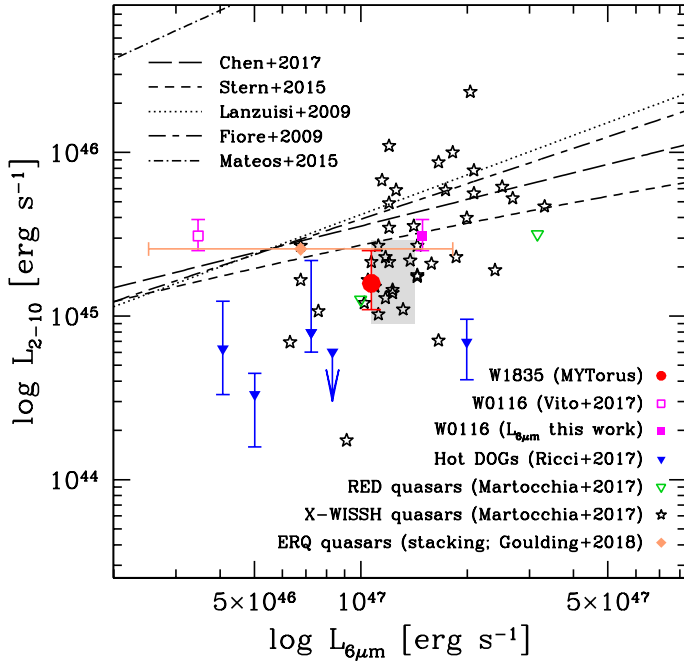
Fig. 5. $L_{6\mu m}$ vs. L_{2-10} relation. The red circle represents W1835 for the MYTORUS geometry (both in X-ray and SED analysis) with the range of systematic uncertainty due to different modelings (see Tables 1 and 3) reported as the gray shaded region. Blue triangles report a compilation of hot DOGs in Ricci et al. (2017a) except for W1835, which we update here. Magenta squares report W0116+0505 with $L_{6\mu m}$ reported by Vito et al. (2018; empty square) or estimated by our SED fitting (filled square; see Sect. 5.1). Black stars and green triangles represent the X-WISSH hyperluminous type I quasar sample (Martocchia et al. 2017) and two reddened quasars (Martocchia et al. 2017). The orange diamond reports the best-fit L_{2-10} value obtained from X-ray spectral analysis performed on a stacked X-ray spectrum of a sample of ERQ sources observed in *Chandra* in Goulding et al. (2018). In the latter, the error bar represents the range of $L_{6\mu m}$ in the sample. We also report X-ray-to-MIR relations derived for different optical/MIR/X-ray selected AGN samples.

ionized halos, which are usually observed in local ultraluminous galaxies (Teng & Veilleux 2010; Jia et al. 2012; Veilleux et al. 2014; Feruglio et al. 2015; Teng et al. 2015). Based on f_{sc} for local low-luminosity AGN, photoionized gas can account for the soft excess. However, this would require a photoionized gas phase emitting with a luminosity on the order of 10^{44} erg s^{-1}, which is a factor of five to one order of magnitude higher than any scattered or photoionized gas phase ever measured in local luminous quasars in the X-rays (Piconcelli et al. 2008; Tazaki et al. 2013; LaMassa et al. 2016). The recent stacking analysis carried out on high-z EQR by Goulding et al. (2018) reported a similarly high (10^{44} erg s^{-1}) scattered component. They used the same MYTOR model as we did, with same assumptions on Γ and torus inclination angle. In order to understand whether these luminous scattered components are indeed associated with photoionized gas, a spectrum with a much higher S/N is needed, hence it is not possible to make such a strong claim. However, there are indications that the photoionized [OIII]-emitting gas that is usually associated with the X-ray emitting gas tends to be lacking or weak in a large fraction (40–70%) of luminous AGN (Netzer et al. 2004; Shen & Ho 2014; Vietri et al. 2018) and is generally more compact than suggested from low-luminosity AGN (Netzer et al. 2004; Bischetti et al. 2017). This has been interpreted as some kind of departure

from the phenomenology reported for less luminous sources (Netzer et al. 2004) and may indicate that the photoionized gas origin is unlikely.

We also evaluated the possibility that the soft-excess emission is due to a collisionally ionized plasma halo. The presence of the ionized Fe line, if confirmed at higher significance than what has been found in P15, may be indicative of high-temperature plasma. If we use a thermal model (APEC in XSPEC) to parameterize the soft excess, we indeed estimate a plasma temperature of $kT \approx 4$ keV. Together with the high luminosity of the soft excess, this may indicate intracluster-medium emission. This result may be tantalizing as hot DOGs have been claimed to be located in overdense galaxy regions (Jones et al. 2014). However, several caveats prevent us from making such a bold claim. The temperature may be driven by the presence of the low-significance putative ionized Fe line reported in P15, whose origin cannot be determined with the current data. Furthermore, as a first-order approximation, the cutoff of the thermal emission and the presence of L-shell Fe lines (a strong temperature indicator for <2 keV plasma) cannot be determined for energies lower than $\sim$2 keV (as we cannot probe rest-frame energies much lower than this value). This means that our data are insensitive to lower temperatures, and we are not able to fully evaluate the parameter space down to lower temperatures.

5.3. Nature of W1835

Recently, Farrah et al. (2017) performed a morphological analysis on HST/WFC3 images of a sample of $z = 2-3$ hot DOGs including W1835 in the optical rest-frame band (*B* band). They found W1835 to have an irregular light profile with no clear close companions. They employed several morphological indicators to quantify its appearance. They found that compared to all the other systems in their sample, the source is less likely to be in a clear merger state according to the boundaries in light concentration, asymmetry, and variance of the brightest 20% of the galaxy light (Conselice et al. 2003; Lotz et al. 2004, 2008). It is therefore possible that either the system is in a non-merger state or in an advanced merger state, showing a common envelope surrounding an unresolved sub-kiloparsec scale nuclear region. Farrah et al. (2017) concluded that there is no need to invoke a preferential link of hot DOGs with mergers, rather ascribing their phenomenology to brief and luminous nuclear accretion episodes in the evolutionary history of a massive star-forming $z \sim 2$ galaxy. A similar analysis carried on by Fan et al. (2016a) instead concluded on a different sample (with very little overlap and including W1835) that hot DOGs are likely a transitional obscured phase in the merger-driven evolutionary QSO formation sequence, leading to the unobscured quasar phase. Interestingly, Ricci et al. (2017b) found from analyzing the X-ray spectra of a sample of luminous and ultra-luminous infrared galaxies in different merging stages that CT AGN that are preferentially hosted in late-stage mergers, with the maximum obscuration reached when the galaxies have projected distances of 0.4–10.8 kpc. In the context of an merger-induced obscuration scenario, W1835 would therefore be interpreted as late-stage merger in which the nucleus is being obscured by infalling matter as a consequence of the loss of angular momentum of the ISM due to the merger phenomenon. However, unless there is a non-AGN-related prominent soft-excess contributor in our X-ray spectrum (i.e., photoionized or collisionally ionized copious amounts of gas), the obscuration cannot be ascribed to an homogeneous 4π obscurer that completely enshrouds the nucleus, as implied by quasar-induced merger formation

scenarios, because the scattered fraction for the spherical obscurer is too high compared to what is typically observed in AGN.

6. Conclusions

We presented a ~155 ks *NuSTAR* observation of the hot DOG W1835. The source was detected with a significance of $3.3\,\sigma$. We extracted *NuSTAR* spectra and jointly modeled them with the *XMM-Newton* spectra that were previously presented in P15. We used both phenomenological and physically motivated models. The latter includes an appropriate treatment of the Compton scattering and accounts for the geometry of the obscurer. We explored two scenarios: 1) an edge-on torus, and 2) a sphere isotropically covering the nucleus. We find that:

– in all cases, a nearly CT $(\log[N_{\rm H}/{\rm cm}^{-2}] \sim 24)$ to heavy CT $(\log[N_{\rm H}/{\rm cm}^{-2}] \gg 24)$ obscuration is required. This makes W1835 the first and most obscured $z > 2$ AGN detected by *NuSTAR* so far;

– W1835 is very luminous and is a Compton-thick quasar, as indicated by the derived unobscured X-ray luminosity $L_{2-10} \approx 1-3 \times 10^{45}$ erg s^{-1} $(L_{10-40} \approx 0.5-2 \times 10^{45}$ erg s$^{-1})$;

– a soft excess at low energies (<2 keV), which may amount to 5–15% of the emission of the primary continuum is also necessary. The uniform spherical model is disfavored because the soft excesses it produces is too high (i.e., >10%), unless a patchy obscurer distribution and/or an uncommon and powerful ($\sim 10^{44}$ erg s^{-1}) non-AGN-related component is invoked.

We further investigated W1835 by performing optical-to-FIR SED modeling with a clumpy two-phase dusty toroidal model accounting for the MIR reprocessed AGN primary emission with the addition of a modified blackbody to model the FIR dust emission primarily heated by stellar processes. In order to be as consistent as possible with the X-ray analysis, we employed similar toroidal and spherical geometrical configurations for the MIR emitter. We found that:

– the source is hyperluminous with a bolometric luminosity of $L_{\rm bol} \approx 3-5 \times 10^{47}$ erg s^{-1};

– the bolometric correction at 2–10 keV (10–40 keV) is on the order of ~300 (~500) and is consistent with those estimated in hyperluminous type I AGN;

– it exhibits a powerful starburst with derived SFRs on the order of ~3000 $M_\odot$ yr^{-1};

– the ratio of X-rays to MIR is higher than the average value for the hot DOGs and is consistent within the uncertainties and accounting for all the modelings with those inferred in type I hyperluminous AGN at the same cosmic epoch.

Considering the heavy obscuration, the luminosity, the ratio of X-rays to MIR, the SFR, and its HST mildly disturbed morphology, this hot DOG can be interpreted as a late-stage merger in the context of the merger-induced quasar formation scenario. It exhibits relatively high values of soft excess, which, if confirmed, may indicate large reservoirs of photoionized or collisionally ionized gas.

Future deep imaging observations of W1835 at higher spatial/spectral resolution both in X-ray (i.e., *Chandra* and *Athena*) and at submillimeter wavelengths (NOEMA) may enable us to further shed light on the nature of W1835.

References

Assef, R. J., Walton, D. J., Brightman, M., et al. 2016, ApJ, 819, 111
Bañados, E., Venemans, B. P., Decarli, R., et al. 2016, ApJS, 227, 11
Banerji, M., Alaghband-Zadeh, S., Hewett, P. C., & McMahon, R. G. 2015, MNRAS, 447, 3368
Beelen, A., Cox, P., Benford, D. J., et al. 2006, ApJ, 642, 694
Bianchi, S., Guainazzi, M., & Chiaberge, M. 2006, A&A, 448, 499
Bianchi, S., Giovanardi, C., Smith, M. W. L., et al. 2017, A&A, 597, A130
Bischetti, M., Piconcelli, E., Vietri, G., et al. 2017, A&A, 598, A122
Brightman, M., & Nandra, K. 2011, MNRAS, 413, 1206
Brightman, M., Nandra, K., Salvato, M., et al. 2014, MNRAS, 443, 1999
Bruzual, G., & Charlot, S. 2003, MNRAS, 344, 1000
Buchner, J., & Bauer, F. E. 2017, MNRAS, 465, 4348
Cash, W. 1979, ApJ, 228, 939
Chabrier, G. 2003, PASP, 115, 763
Chen, C.-T. J., Hickox, R. C., Goulding, A. D., et al. 2017, ApJ, 837, 145
Conselice, C. J., Bershady, M. A., Dickinson, M., & Papovich, C. 2003, AJ, 126, 1183
Delvecchio, I., Gruppioni, C., Pozzi, F., et al. 2014, MNRAS, 439, 2736
Dey, A., Soifer, B. T., Desai, V., et al. 2008, ApJ, 677, 943
Di Matteo, T., Springel, V., & Hernquist, L. 2005, Nature, 433, 604
Duras, F., Bongiorno, A., Piconcelli, E., et al. 2017, A&A, 604, A67
Eisenhardt, P. R. M., Wu, J., Tsai, C.-W., et al. 2012, ApJ, 755, 173
Fabian, A. C. 1999, MNRAS, 308, L39
Fabian, A. C., Lohfink, A., Kara, E., et al. 2015, MNRAS, 451, 4375
Fan, L., Han, Y., Fang, G., et al. 2016a, ApJ, 822, L32
Fan, L., Han, Y., Nikutta, R., Drouart, G., & Knudsen, K. K. 2016b, ApJ, 823, 107
Fan, X., Narayanan, V. K., Lupton, R. H., et al. 2001, AJ, 122, 2833
Fan, X., Strauss, M. A., Schneider, D. P., et al. 2003, AJ, 125, 1649
Farrah, D., Petty, S., Connolly, B., et al. 2017, ApJ, 844, 106
Feltre, A., Hatziminaoglou, E., Fritz, J., & Franceschini, A. 2012, MNRAS, 426, 120
Feruglio, C., Fiore, F., Maiolino, R., et al. 2013, A&A, 549, A51
Feruglio, C., Bongiorno, A., Fiore, F., et al. 2014, A&A, 565, A91
Feruglio, C., Fiore, F., Carniani, S., et al. 2015, A&A, 583, A99
Fiore, F., Puccetti, S., Brusa, M., et al. 2009, ApJ, 693, 447
Fritz, J., Franceschini, A., & Hatziminaoglou, E. 2006, MNRAS, 366, 767
Gandhi, P., Horst, H., Smette, A., et al. 2009, A&A, 502, 457
Gehrels, N. 1986, ApJ, 303, 336
Glikman, E., Urrutia, T., Lacy, M., et al. 2012, ApJ, 757, 51
Goulding, A. D., Zakamska, N. L., Alexandroff, R. M., et al. 2018, ApJ, 856, 4
Guainazzi, M., & Bianchi, S. 2007, MNRAS, 374, 1290
Harrison, F. A., Craig, W. W., Christensen, F. E., et al. 2013, ApJ, 770, 103
Heckman, T. M., & Best, P. N. 2014, ARA&A, 52, 589
Hopkins, P. F., Hernquist, L., Cox, T. J., et al. 2006, ApJS, 163, 1
Hopkins, P. F., Richards, G. T., & Hernquist, L. 2007, ApJ, 654, 731
Hopkins, P. F., Hernquist, L., Cox, T. J., & Kereš, D. 2008, ApJS, 175, 356
Huang, J.-S., Rigopoulou, D., Magdis, G., et al. 2014, ApJ, 784, 52
Jia, J., Ptak, A., Heckman, T. M., Braito, V., & Reeves, J. 2012, ApJ, 759, 41
Jones, S. F., Blain, A. W., Stern, D., et al. 2014, MNRAS, 443, 146
Kennicutt, R. C., Jr 1998, ARA&A, 36, 189
Kennicutt, R. C., & Evans, N. J. 2012, ARA&A, 50, 531
King, A. 2003, ApJ, 596, L27
Kormendy, J., & Ho, L. C. 2013, ARA&A, 51, 511
LaMassa, S. M., Ricarte, A., Glikman, E., et al. 2016, ApJ, 820, 70
Lanzuisi, G., Piconcelli, E., Fiore, F., et al. 2009, A&A, 498, 67
Lanzuisi, G., Ranalli, P., Georgantopoulos, I., et al. 2015, A&A, 573, A137
Lotz, J. M., Primack, J., & Madau, P. 2004, AJ, 128, 163
Lotz, J. M., Davis, M., Faber, S. M., et al. 2008, ApJ, 672, 177
Lusso, E., Comastri, A., Simmons, B. D., et al. 2012, MNRAS, 425, 623
Madsen, K. K., Harrison, F. A., Markwardt, C. B., et al. 2015, ApJS, 220, 8
Magnelli, B., Lutz, D., Santini, P., et al. 2012, A&A, 539, A155
Martocchia, S., Piconcelli, E., Zappacosta, L., et al. 2017, A&A, 608, A51
Mateos, S., Carrera, F. J., Alonso-Herrero, A., et al. 2015, MNRAS, 449, 1422
Menci, N., Fiore, F., Puccetti, S., & Cavaliere, A. 2008, ApJ, 686, 219
Merloni, A., & Heinz, S. 2008, MNRAS, 388, 1011
Murphy, K. D., & Yaqoob, T. 2009, MNRAS, 397, 1549

Nandra, K., O'Neill, P. M., George, I. M., & Reeves, J. N. 2007, MNRAS, 382, 194

Narayanan, D., Dey, A., Hayward, C. C., et al. 2010, MNRAS, 407, 1701

Netzer, H., Shemmer, O., Maiolino, R., et al. 2004, ApJ, 614, 558

Piconcelli, E., Bianchi, S., Miniutti, G., et al. 2008, A&A, 480, 671

Piconcelli, E., Vignali, C., Bianchi, S., et al. 2015, A&A, 574, L9

Pozzi, F., Vignali, C., Comastri, A., et al. 2007, A&A, 468, 603

Ranalli, P., Comastri, A., & Setti, G. 2003, A&A, 399, 39

Ricci, C., Assef, R. J., Stern, D., et al. 2017a, ApJ, 835, 105

Ricci, C., Bauer, F. E., Treister, E., et al. 2017b, MNRAS, 468, 1273

Richards, G. T., Strauss, M. A., Fan, X., et al. 2006, AJ, 131, 2766

Sanders, D. B., Soifer, B. T., Elias, J. H., et al. 1988, ApJ, 325, 74

Schawinski, K., Simmons, B. D., Urry, C. M., Treister, E., & Glikman, E. 2012, MNRAS, 425, L61

Schawinski, K., Koss, M., Berney, S., & Sartori, L. F. 2015, MNRAS, 451, 2517

Shen, Y., & Ho, L. C. 2014, Nature, 513, 210

Silk, J., & Rees, M. J. 1998, A&A, 331, L1

Stalevski, M., Ricci, C., Ueda, Y., et al. 2016, MNRAS, 458, 2288

Stern, D. 2015, ApJ, 807, 129

Stern, D., Lansbury, G. B., Assef, R. J., et al. 2014, ApJ, 794, 102

Tazaki, F., Ueda, Y., Terashima, Y., Mushotzky, R. F., & Tombesi, F. 2013, ApJ, 772, 38

Teng, S. H., & Veilleux, S. 2010, ApJ, 725, 1848

Teng, S. H., Rigby, J. R., Stern, D., et al. 2015, ApJ, 814, 56

Treister, E., Schawinski, K., Urry, C. M., & Simmons, B. D. 2012, ApJ, 758, L39

Tsai, C.-W., Eisenhardt, P. R. M., Wu, J., et al. 2015, ApJ, 805, 90

Urrutia, T., Lacy, M., & Becker, R. H. 2008, ApJ, 674, 80

Urry, C. M., & Padovani, P. 1995, PASP, 107, 803

Valiante, R., Schneider, R., Salvadori, S., & Gallerani, S. 2014, MNRAS, 444, 2442

Veilleux, S., Teng, S. H., Rupke, D. S. N., Maiolino, R., & Sturm, E. 2014, ApJ, 790, 116

Vietri, G., Piconcelli, E., Bischetti, M. 2018, A&A, 617, A81

Vito, F., Brandt, W.N., Stern, D. 2018, MNRAS, 474, 4528

Volonteri, M., Salvaterra, R., & Haardt, F. 2006, MNRAS, 373, 121

Wachter, K., Leach, R., & Kellogg, E. 1979, ApJ, 230, 274

Weedman, D., Sargsyan, L., Lebouteiller, V., Houck, J., & Barry, D. 2012, ApJ, 761, 184

Wik, D. R., Hornstrup, A., Molendi, S., et al. 2014, ApJ, 792, 48

Willott, C. J., Delorme, P., Reylé, C., et al. 2010, AJ, 139, 906

Wright, E. L., Eisenhardt, P. R. M., Mainzer, A. K., et al. 2010, AJ, 140, 1868

Wu, J., Tsai, C.-W., Sayers, J., et al. 2012, ApJ, 756, 96

Yaqoob, T. 2012, MNRAS, 423, 3360

Zappacosta, L., Comastri, A., Civano, F., et al. 2018, ApJ, 854, 33